

# Insertion space in repulsive active matter

Luke K. Davis<sup>1, 2, 3, \*</sup> and Karel Proesmans<sup>4</sup>

<sup>1</sup>School of Mathematics and Maxwell Institute for Mathematical Sciences, University of Edinburgh, EH9 3FD, Scotland

<sup>2</sup>Higgs Centre for Theoretical Physics, University of Edinburgh, EH9 3FD, Scotland

<sup>3</sup>Isaac Newton Institute for Mathematical Sciences, University of Cambridge, CB3 0EH, England

<sup>4</sup>Niels Bohr International Academy, Niels Bohr Institute, Blegdamsvej 17, DK-2100 Copenhagen

For equilibrium hard spheres the stochastic geometry of the insertion space, the room to accommodate another sphere, relates exactly to the equation of state. We begin to extend this idea to active matter, analyzing insertion space for repulsive active particles in one and two dimensions using both on- and off-lattice models. In 1D we derive closed-form expressions for the mean insertion cavity size, cavity number, and total insertion volume, all in excellent agreement with simulations. Strikingly, activity increases the total insertion volume and tends to keep the insertion space more connected. These results provide the first quantitative foundation for the stochastic geometry of active matter, and opens up a new route to building a thermodynamics of active systems.

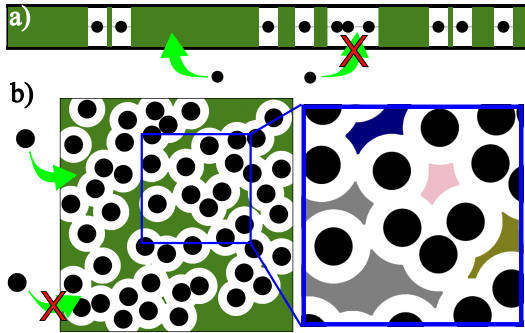


FIG. 1. a) Visualized insertion cavities for a configuration of hard spheres in  $d = 1$ . b) Example insertion cavities for a configuration of hard discs in a closed box. Disconnected cavities identified in our algorithm (right).

Most people encounter the idea of insertion as children, through the playing of shape sorting blocks or other such toys. Insertion is one of the most basic actions in the natural and human worlds: it is the act of storing physical objects in space. The practical difficulty of insertion lies in objects taking up a limited amount of space and accounting for the many ways to arrange the objects (Fig. 1). Typically, the objects of insertion are treated as non-motile and in equilibrium [1, 2], but what happens if they are, instead, motile and far-from-equilibrium? Here, we provide the first answer to this question in the context of active matter: a broad class of non-equilibrium systems whose constituents turnover energy to fuel their dynamics [3]. Understanding insertion has important practical ramifications regarding the storage of active units, such as self-propelled colloids [4], robots [5], and motile cells [6], which could form the next generation of engines [7].

Active constituents interact in many ways, with volume-exclusion (a form of repulsion) being the most relevant for insertion [8–10]. An important phenomenon that arises for active—as opposed to passive—repulsive par-

ticles is motility-induced phase separation (MIPS): the formation of dense clusters of particles surrounded by a dilute vapor [11]. The non-equilibrium driving and the many-body repulsive interactions make understanding the insertability of active matter difficult.

It has been shown that some frameworks and ideas from equilibrium statistical mechanics, *i.e.* of passive matter, can be leveraged to understand the thermodynamics of active matter [12]. Motivated by these successes, we here begin to investigate an unexplored avenue: the relationship between thermodynamics and insertion space (IS), or, in general, stochastic geometry, that was established for equilibrium hard-spheres [13–19]. Remarkably, there exist *exact* relations, attributed to R. J. Speedy, connecting both the equilibrium compressibility  $Z = \beta PV/N$  and, separately, the total chemical potential  $\mu$  to the averaged insertion space (IS), *i.e.*, the room available to place another sphere averaged over all configurations [13] (Fig. 1):

$$Z_G := 1 + \frac{\sigma \langle S_I \rangle}{2d \langle V_I \rangle}, \quad \mu_G := -\ln \frac{\langle V_I \rangle}{V}, \quad (1)$$

$$Z_G = Z \equiv \beta PV/N, \quad \mu_G = \mu_{\text{exc}} = \beta \mu - \ln \frac{N \Lambda^d}{V} \quad (2)$$

At equilibrium

where  $\beta = (k_B T)^{-1}$  is the inverse temperature,  $P$  is the bulk pressure,  $V$  is the total volume of the space,  $N$  is the number of constituents,  $\sigma$  is the particle diameter (or repulsion range),  $d$  is the spatial dimension,  $\Lambda$  is the thermal de Broglie wavelength,  $\langle V_I \rangle$  is the averaged (over all values in all configurations) total insertion volume, and  $\langle S_I \rangle$  its averaged concomitant surface. The insertion volume is expressed in terms of the averaged (over all values across all configurations) number of cavities and cavity size as  $\langle V_I \rangle = \langle N_\Delta \rangle \langle \Delta \rangle$  [15, 17].

The appeal of the above relations, is that—at equilibrium—each of the LHS of (1) have clear thermodynamic interpretations (2) while the RHS of (1) are purely geometric. However, it is not straightforward how one should view the above relations in light of active matter: systems far from equilibrium. Already, it has been

\* Correspondence: luke.davis@ed.ac.uk

shown that an equation of state,  $Z$ , with the equilibrium interpretation, is the exception and not the rule for active systems [20]. Thus, if (2) were to somehow hold the interpretation of the thermodynamic objects must change. Though, before this, a systematic investigation into the geometric objects in (1) for active systems needs to be done. An important anchoring point is that the determination and interpretation of the IS quantities are purely geometric, and remain concrete far away from equilibrium. Here, we determine the IS and its statistics for repulsive active matter models in low dimensions.

Firstly, in  $d = 1$ , the dimensionless averaged cavity size  $\langle \Delta \rangle / \sigma \equiv \langle \tilde{\Delta} \rangle$  is the free (unoccupied) space divided by the number of non-touching particle pairs minus one and reads as:

$$\langle \tilde{\Delta} \rangle = \frac{1 + \eta(P_C - 2)}{\eta(1 - P_C)}, \quad (3)$$

where  $P_C$  is the probability of two particles being in contact and  $\eta = N\sigma/V$  is the packing fraction. In one dimension,  $\langle S_I \rangle = 2\langle N_\Delta \rangle$  exactly, implying that the geometric compressibility  $Z_G$  (1) can be simplified as [13]

$$Z_G = 1 + \langle \tilde{\Delta} \rangle^{-1}. \quad (4)$$

The averaged total number of cavities  $\langle N_\Delta \rangle$  can be written in terms of  $P_C$  as

$$\langle N_\Delta \rangle = N(1 - P_C), \quad (5)$$

with  $\langle N_\Delta \rangle = N$  in the dilute limit and  $\langle N_\Delta \rangle = 0$  at full packing ( $\eta = 1$ ). The averaged total insertion volume is then, as a function of  $P_C$ ,

$$\langle V_I \rangle = V + N\sigma(P_C - 2), \quad (6)$$

with  $\langle V_I \rangle = V - N(2\sigma)$  in the dilute case, where  $2\sigma$  is the volume excluded by one particle, and  $\langle V_I \rangle = 0$  at full packing. Note, that  $P_C$  is absent in the original expressions of these quantities [13]. The equilibrium one-dimensional hard-sphere model is the Tonks gas, which is exactly solvable [8], where the IS quantities are given exactly as [14, 15]:

$$\begin{aligned} \langle \tilde{\Delta} \rangle_0 &= \frac{(1 - \eta)}{\eta}, \quad \langle N_\Delta \rangle_0 = N \exp\left(-\frac{1}{\langle \tilde{\Delta} \rangle_0}\right), \\ \langle V_I \rangle_0 &= V(1 - \eta) \exp\left(-\frac{1}{\langle \tilde{\Delta} \rangle_0}\right), \end{aligned} \quad (7)$$

with a corollary that  $P_C^{\text{eq}} = 1 - \exp(-\langle \tilde{\Delta} \rangle_0^{-1})$ .

For the active model we consider repulsive run-and-tumble particles (RTPs) in  $d = 1$ . The model consists of  $N$  RTPs, of diameter  $\sigma$ , on a lattice of  $n = V/\sigma \in \mathbb{Z}^+$  sites. In this model the run durations  $k_i$ , for particle  $i$ , are exponentially distributed with rate-parameter  $K^{-1} \geq 0$  and, during the runs, the particles have a constant self-propulsion speed  $v_0$  [21]. At passivity ( $K \rightarrow 0$ ) the model reduces to the simple symmetric exclusion process (SSEP) [22]. The RTP particle model can be mapped to a mass transfer model with

fluctuating directed bonds (as is done in the Dandekar-Chakraborti-Rajesh (DCR) model [23]), which we exploit here. The neighboring probability  $P_C$  can be broken down as  $4P_C = p_{\rightarrow,\leftarrow} + 2p_{\rightarrow,\rightarrow} + p_{\leftarrow,\rightarrow}$ , where  $p_{\rightarrow,\leftarrow}$  is the probability that two particles are next to each other with the left one moving right and the right one moving left,  $p_{\rightarrow,\rightarrow} = p_{\leftarrow,\leftarrow}$  is the probability that two particles are next to each other where both particles move in the same direction, and  $p_{\leftarrow,\rightarrow}$  is the probability to be next to each other with the left particle moving left and the right particle moving right. The expressions for  $p_{\rightarrow,\leftarrow}$ ,  $p_{\rightarrow,\rightarrow}$  and  $p_{\leftarrow,\rightarrow}$  are difficult to obtain exactly, and so we resort to a mean-field approximation (A1) (as is done in [23]). For weak activity, *i.e.*,  $K \lesssim 1$ , the mean-field  $P_C$  reads (up to  $O(K^3)$ ) as,

$$P_C \underset{K \lesssim 1}{=} \eta + \frac{\eta(\eta - 1)^2 K}{2} + \frac{(\eta - 1)^2 \eta(4\eta^2 - 7\eta + 1) K^2}{8}. \quad (8)$$

For the high-activity (large persistence) regime naively expanding  $P_C$  for small  $K^{-1} \ll 1$  is pathological (as noted in [23]). The main reason for this is that the mean-field treatment assumes bonds (orientations between close particles) as independent and thus cannot-by design-represent the long, strongly correlated domains of like orientation that arise at large persistence. A better high-activity starting point is the coalescence-fragmentation picture in the DCR model (section IV of [23]) which focuses on the interfaces of co-moving particle clusters. In this picture, in the steady-state, there is a balance in the rates of clusters joining and breaking resulting in the density of interfacial bonds (jammed interfaces) going as  $\zeta^* = \sqrt{K^{-1}\langle \tilde{\Delta} \rangle_0}$  and the typical unoccupied cavity size going as  $K\zeta^*$ . Then the contact probability is simply  $P_C \underset{K \gg 1}{=} 1 - \zeta^*$ . In the full packing regime both the weak and high activity limits obey  $P_C(\eta \rightarrow 1) = 1$ , yet in the dilute regime  $P_C(\eta \rightarrow 0) \sim 0$  for  $K \rightarrow 0$  while  $P_C(\eta \rightarrow 0) \sim \mathcal{O}(1)$  for  $K \rightarrow \infty$  (high persistence limit taken first).

The dimensionless averaged cavity size (3) in the presence of weak and strong activity is then, respectively,

$$\begin{aligned} \langle \tilde{\Delta} \rangle &\underset{K \lesssim 1}{=} \langle \tilde{\Delta} \rangle_0 + \frac{K}{2}(1 - \eta) - \frac{K^2(1 - \eta)(1 - 5\eta + 2\eta^2)}{8}, \\ \langle \tilde{\Delta} \rangle &\underset{K \gg 1}{=} K\zeta^* - 1 \equiv \sqrt{K\langle \tilde{\Delta} \rangle_0} - 1, \end{aligned} \quad (9)$$

with  $\langle N_\Delta \rangle$  and  $\langle V_I \rangle$ , also given, respectively, as:

$$\begin{aligned} \frac{\langle N_\Delta \rangle}{N} &\underset{K \lesssim 1}{=} (1 - \eta) - \frac{K\eta(1 - \eta)^2}{2} \left(1 - \frac{K(1 - 7\eta + 4\eta^2)}{4}\right), \\ \frac{\langle N_\Delta \rangle}{N} &\underset{K \gg 1}{=} \zeta^* \equiv \sqrt{K^{-1}\langle \tilde{\Delta} \rangle_0}, \end{aligned} \quad (10)$$

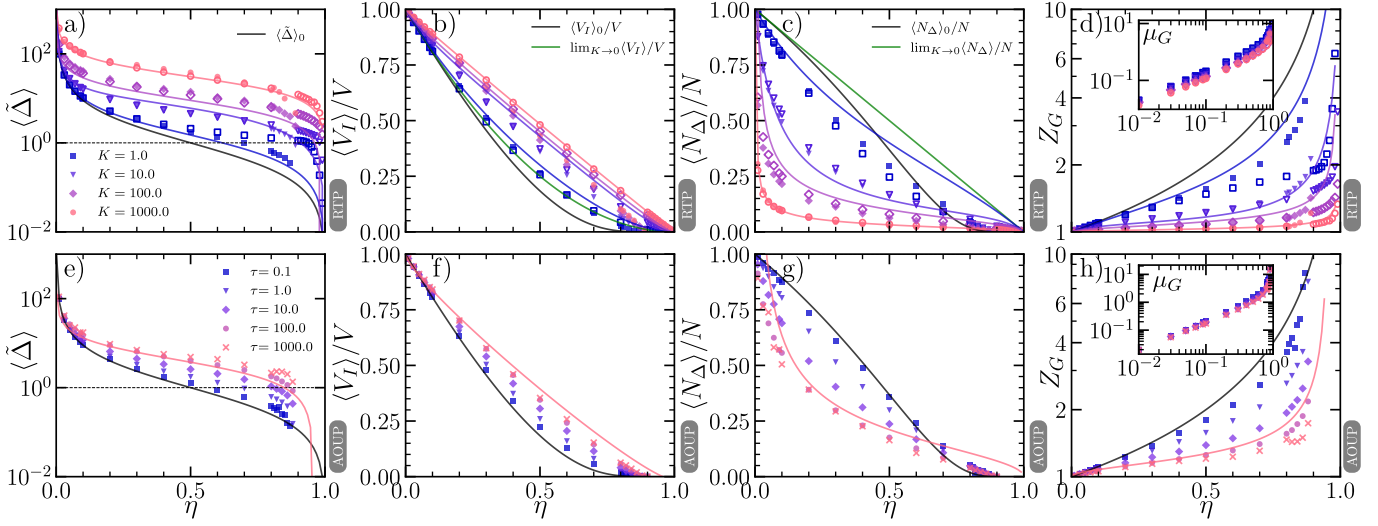


FIG. 2. Insertion space (IS) for repulsive active particles in  $d = 1$ . a) Averaged normalized cavity size as a function of packing fraction  $\eta$ , as determined from off-lattice (filled points) and on-lattice (unfilled points) simulations of RTPs at various  $K$ . Analytical results are solid lines; for  $K \leq 10.0$  the lines are the weak activity mean-field expressions while for  $K > 10.0$  we show the high-activity expressions (9-11). Exact passive expressions are from (7). b) The averaged total insertion volume divided by the system volume. c) Averaged number of insertion cavities per particle as a function of  $\eta$ . d) The geometric compressibility,  $Z_G$ , as a function of  $\eta$ . Inset is the geometric chemical potential  $\mu_G$  against  $\eta$ . e) - h) The same quantities as for a)-d) but for the AOUPl (off-lattice) model. High-activity analytics (for  $\tau = 1000$ ) are (9-11) with  $K \simeq \sqrt{D'\tau}/\sigma$ . Parameters (RTPs):  $N = 1024$ ,  $\mu = 1$  (off-lattice),  $\epsilon = 10$  (off-lattice), and  $\sigma = 1$ ; AOUPls:  $N = 1024$ ,  $\mu = 1$ ,  $\epsilon = 10$ ,  $D' = \frac{1}{2}$  and  $\sigma = 1$ .

and

$$\begin{aligned} \frac{\langle V_I \rangle}{V} &\underset{K \lesssim 1}{=} (1 - \eta)^2 \left( 1 + \frac{K\eta}{2} + \frac{K^2\eta(1 - 7\eta + 4\eta^2)}{8} \right), \\ \frac{\langle V_I \rangle}{V} &\underset{K \gg 1}{=} 1 - \eta(1 + \zeta^*) \equiv 1 - \eta \left( 1 + \sqrt{K^{-1}\langle \tilde{\Delta} \rangle_0} \right). \end{aligned} \quad (11)$$

These relations have two strong physical implications: (i) the relations (9) show that to leading order—the averaged cavity size is always higher at higher activity, (ii) (10) imply that the presence of activity tends to reduce, relative to the passive case, the total number of insertion cavities, and (iii) relations (11) imply that the presence of activity increases, relative to equilibrium, the averaged total insertion space across the entire packing fraction. Another way to think of this is through the increased probability of insertion  $\mathcal{P}_I \equiv \langle V_I(K, \eta) \rangle / V$ . Moreover, in the limit of extreme activity ( $K \rightarrow \infty$ ), we obtain a rather simple relationship  $\langle V_I \rangle / V \propto -\eta$  which is even simpler than both the exact and mean-field-limit equilibrium expressions. Due to  $\langle \tilde{\Delta} \rangle > \langle \tilde{\Delta} \rangle_0$ , for  $K > 0$ , we predict a lower  $Z_G$  across the full range of  $\eta$ . Interestingly, in the limit  $\lim_{K \rightarrow \infty} Z_G = 1$  which is equivalent to the compressibility for an equilibrium ideal gas. Additionally, we predict a lower geometric chemical potential  $\mu_G$  on the basis that  $\langle V_I(K, \eta) \rangle > \langle V_I(\eta) \rangle_0 \forall K, \eta$ . These insights and the writing down of the relations (9-11) are our main theoretical results.

To test our theoretical predictions (9-11) we perform on- and off-lattice numerical simulations of repulsive RTPs in  $d = 1$  (Fig. 2). The implementation of the

on-lattice model consists of RTPs hopping between adjacent sites and tumbling at exponentially-sampled rates with rate parameter  $K^{-1}$ , with a successful move to a new site only if that site is unoccupied. The off-lattice model has essentially the same ingredients, with the exception of continuous space and strict volume-exclusion being modeled by a repulsive (WCA) potential (see the dynamics (B1) and Appendix B). In the simulations, for a given configuration  $\omega$  the IS can be quantified through the insertion profile (Fig. D.1) which reads as:

$$\rho_I(x; \omega) := 1 - \Theta \left( \sum_{i=1}^N \Theta(\sigma - |x - x_i|) \right), \quad (12)$$

where  $\Theta(\dots)$  is the Heaviside function. By assuming that particles are ordered on the line as  $i = 1, \dots, N$ , then the insertion cavity  $\tilde{\Delta}_{i,i+1}(\omega)$ , between two neighboring particles  $i$  and  $i + 1 \bmod N$ , the instantaneous number of insertion cavities per particle  $N_\Delta(\omega)/N$ , and the total insertion space  $V_I(\omega)/V$  are exactly determined as:

$$\begin{aligned} \tilde{\Delta}_{i,i+1}(\omega) &= \frac{\text{sgn}(x'_{i+1} - x'_i)}{\sigma} \int_{x'_i}^{x'_{i+1}} \rho_I(x; \omega) dx, \\ \frac{N_\Delta(\omega)}{N} &= \frac{1}{N} \sum_{i=1}^N \Theta(\tilde{\Delta}_{i,i+1}(\omega)), \quad \frac{V_I(\omega)}{V_{d=1}} = \frac{1}{V} \int_0^V \rho_I(x) dx, \end{aligned} \quad (13)$$

where  $x'_i$  denotes the wrapped coordinate for  $i$ .

Our numerical results are, on the whole, in very good agreement with the theoretical mean-field predictions (Fig. 2). For  $\langle \tilde{\Delta} \rangle$  the agreement between the on- and off-lattice simulations is excellent for  $\eta \lesssim 0.5$  but worsens for both higher  $\eta$  and lower  $K$  (Fig. 2(a)). The reason for the former is that at higher packing, the off-lattice simulations are able to better sample smaller (than  $\sigma = 1$ ) insertion cavities which is difficult in the on-lattice simulations with a single-site per particle. For the diminishing discrepancy at higher  $K$ : for a particular  $\eta$  the increase in activity increases the mean cavity size, which tends to be higher than  $\sigma$  and which the on-lattice simulations are better able to sample, however as the system becomes more dense the average cavity size will naturally start to shrink where, again, the on-lattice simulations will struggle to sample these lower values. As expected, as the activity weakens, with  $K \rightarrow 0$ , the data approaches the known passive result  $\langle \tilde{\Delta} \rangle_0$  (7) (see also leading order term of weak-activity expression (9)).

Gratifyingly, the numbers for  $\langle V_I \rangle / V$  (Fig. 2(b)) at high-activity align excellently with our prediction that  $\langle V_I \rangle / V \propto -\eta$ . We note that the passive limit of (11) is in much better agreement for the  $K = 1.0$  data than the full weak-activity expression (up to  $\mathcal{O}(K^3)$ ), this suggests that (at  $K = 1$ ) all  $K$ -terms should approximately cancel to leave  $\langle V_I \rangle / V = (1 - \eta)^2$ . For the averaged number of insertion cavities  $\langle N_\Delta \rangle / N$  (Fig. 2(c)) we note the excellent agreement between the simulations and the mean-field prediction, which increasingly worsens for lower  $K$ . Interestingly, at higher activity, *e.g.*,  $K = 1000$ , there is a rapid decline of the number of insertion cavities at small  $\eta$  which then flattens out. The interpretation of this is that the insertion space tries to be as connected (in the percolation sense) as possible. We find that both the geometric compressibility and geometric chemical potential are lower for higher  $K$  (Fig. 2(d)). Lastly, we found that, out-of-equilibrium, care must be taken with the averaging, where naive averages of  $N_\Delta$  and  $\Delta$  are no longer statistically independent (see Appendix E and Fig. E.1).

We next wondered whether our insights carried over to a different model of repulsive active matter. Thus, we performed off-lattice numerical simulations of repulsive active Ornstein Uhlenbeck particles (AOUPS) in one-dimension (see Appendix C). To tune activity we varied the persistence time of the OU process  $\tau$ , with passivity taken at  $\tau \rightarrow 0$ . Overall, we find that the insertion space in the AOUP case closely follows that for RTPs: the average insertion cavity and averaged total insertion volume are always higher for increasing activity, whilst the averaged number of cavities, geometric compressibility, and geometric chemical potential tend to decrease with activity (see Fig. 2). To our surprise, we find that the high activity expressions of the IS observables of  $\langle \tilde{\Delta} \rangle$  (9-11) with the replacement  $K = \sqrt{D' \tau} / \sigma$ , derived for an on-lattice RTP model, quantitatively describes the off-lattice AOUP numerical data for  $\tau = 1000$  almost as well as the off-lattice RTP data.

Thus far, we have only considered one spatial dimension.

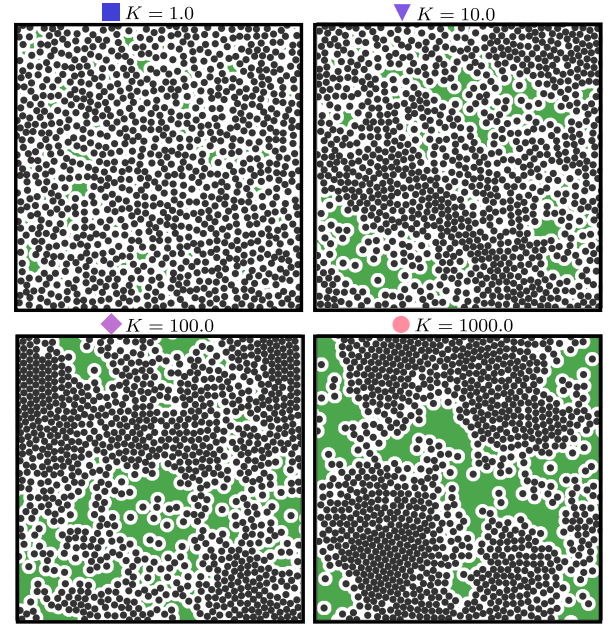


FIG. 3. Snapshots from two-dimensional off-lattice simulations of RTPs and insertion cavities for varying  $K$  at  $\eta = 0.4$ .

tion. We now determine how the insertion space changes for repulsive active particles in  $d = 2$ . Analytical results in higher dimensions present significant challenges, even in equilibrium. The mathematical challenge is that, unlike in  $d = 1$ , different particles can form the boundary of a single cavity and thus cavities cannot be labeled by particle indices consistently between different configurations. One certain difference in higher dimensions is that the number of cavities per particle approaches (in the dilute limit)  $\langle N_\Delta \rangle \rightarrow 1$ , in contrast with  $\langle N_\Delta \rangle \rightarrow N$  for  $d = 1$  [16]. Another fact is that  $\langle S_I \rangle / \langle N_\Delta \rangle$ , the typical surface area of the insertion cavity, is not a priori a constant.

As there are no analytical relations (on the lattice) in  $d = 2$  we here only perform off-lattice simulations [24]. The dynamics of RTPs and AOUPs are, respectively, (B1) and (C1) with  $d = 2$ . In higher dimensions the determination of the IS is nontrivial. Here we develop a conceptually simple and efficient voxel-based algorithm to determine the IS quantities, which is straightforward to parallelize and also extend to higher dimensions (see Appendix F). In short, our algorithm partitions the space into voxels of side length  $l \ll V^{1/2}$  and removes voxels inside the exclusion zones of particles. If implemented naively (comparing each voxel with every particle) the algorithm is incredibly slow, to avoid this we only check the voxels surrounding the particles and leverage the symmetry of the sphere and cube, greatly improving the complexity and attainable resolution (Fig. F.1). We show the convergence of our method in (Fig. F.2). Whilst exact algorithms based on voronoi constructions exist [17, 25, 26], they are not as easy to implement and to extend to higher dimensions [27].

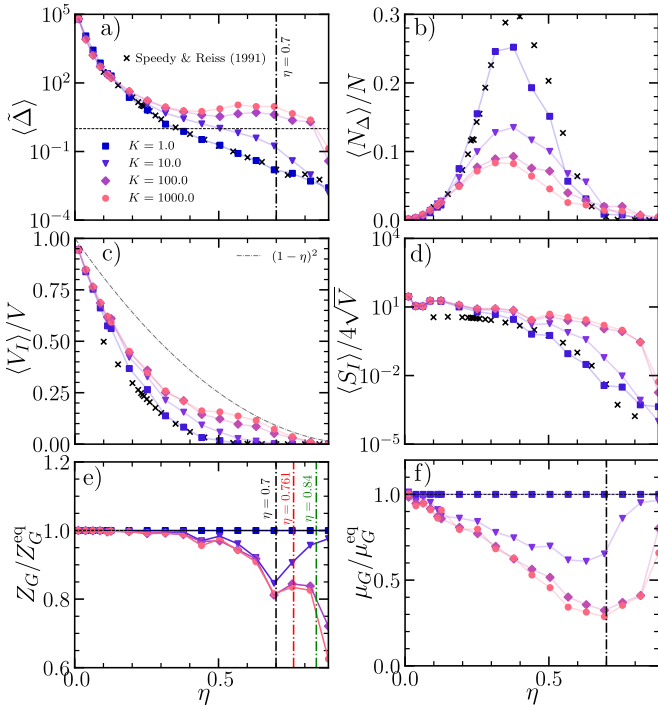


FIG. 4. Quantification of the insertion space for off-lattice simulations of repulsive RTPs in  $d = 2$ . a) Averaged insertion cavity size as a function of  $\eta$ . Hard disc equilibrium data from [16] are shown as reference. b) Number of insertion cavities per particle. c) Averaged total insertion volume. d) The boundary of the insertion volume. e)  $Z_G$  (1) as compared to passivity. The packing fraction  $\eta = 0.7$  is within 5% of the freezing transition [28] and also the location of liquid-hexatic coexistence at low  $Pe$  [29],  $\eta = 0.761$  is the packing fraction at which the hard-disc fluid freezes [16, 30],  $\eta = 0.84$  is the predicted packing fraction at which the metastable fluid to maximally random jammed state transition occurs [31]. f) The geometric chemical potential compared to passivity.

Crucially, the off-lattice simulations of RTPs in  $d = 2$  still show that the total insertion space remains higher and tends to be more connected as compared with equilibrium (Figs. 3 and 4). Interestingly, we find that, at high activities  $K > 10$ ,  $\langle \tilde{\Delta} \rangle$  no longer remains strictly monotonic (as in  $d = 1$ ) with a wide shelf between  $\eta = 0.5 - 0.75$  (Fig. 4a)). As expected, our close-to-equilibrium data  $K \approx 1$  is in excellent agreement with previous IS quantifications in equilibrium hard disc simulations [16]. We observe a tendency for lower averaged number of insertion cavities at higher  $K$ , with a  $\gtrsim 2$ -fold decrease in the maximum at our highest explored activity (Fig. 4b)). Interestingly, the maximum of  $\langle N_\Delta \rangle$  is approximately the same as in equilibrium  $\eta = 0.3 - 0.4$  [16]. For the boundary of the insertion space  $\langle S_I \rangle$  we find it to be a monotonically decreasing function of  $\eta$  (due to periodic boundaries) and generally higher for higher activity,

though some saturation appears for very high activities  $K \geq 100$  (Fig. 4d)). For the geometric compressibility  $Z_G$  we find that the equilibrium  $Z_G^{\text{eq}}$  well approximates the active data for low packing  $\eta < 0.4$ , but then starts to rapidly deviate to lower values (Fig. 4e)). Interestingly, close to known values of phase transitions (freezing [28] and liquid-hexatic coexistence [29]),  $\eta \gtrsim 0.7$ , we find that the slope of  $Z_G/Z_G^{\text{eq}}$  abruptly changes sign. Only for the high activity data does it again change sign, at  $\eta \approx 0.8$ . There is a concomitant change of sign in the geometric chemical potential  $\mu_G/\mu_G^{\text{eq}}$  (Fig. 4f)).

In this letter, we have made the first analytical and numerical investigations into the insertion space of volume-excluding (repulsive) active matter. We show that, across the entire range of packing fractions, the total insertion space is *always* higher in the presence of activity, however weak or strong. This fact is borne out in analytics and simulations for two different well-studied particle models of active matter: RTPs and AOUPs. We expect that our findings to be true for different models of repulsive active matter. We have discovered that activity tends to reduce the total number of insertion cavities, implying that the insertion space remains more connected. Importantly, our results and predictions regarding the insertion space of active matter are clearly experimentally testable, and could be tested in systems of monodisperse active colloids. Future work, and challenges, include a systematic investigation comparing mechanical definitions of compressibility, pressure, and chemical potential in active systems [20, 32–35]. Further, it is not exactly clear how the increased (active) insertion volume should relate to mechanical explanations of MIPS: the slowing down of particles with density results in instabilities that favor clustering [11]. Other questions are: how is the insertion space related to both the degree of time irreversibility and the entropy production [36]? Can the active insertion space reveal the thermodynamic phases of active matter [37]? Remaining technical challenges are to find exact, rather than perturbative, relations for the insertion space in one-dimension and to explore higher dimensions  $d = 3$ . We also wonder how the insertion space behaves in the context of other active matter systems, such as non-reciprocal active matter [38], and how it could inform the control of active matter [39].

*Acknowledgments:-* We thank Prashant Singh, Mike Cates, and Rob Jack for early discussions. L.K.D. acknowledges the Flora Philip Fellowship at the University of Edinburgh and funding from the Isaac Newton Institute for Mathematical Sciences Postdoctoral Research Fellowship (EPSRC Grant Number EP/V521929/1). L.K.D. thanks the Rosenfeld Foundation for supporting a visit to the NBI, Copenhagen. L.K.D. acknowledges the use of the Edinburgh Compute and Data Facility (ECDF).

---

[1] B. Widom, Some topics in the theory of fluids, *The Journal of Chemical Physics* **39**, 2808–2812 (1963).

[2] R. J. Speedy, Accurate theory of the hard sphere fluid, *Journal of the Chemical Society, Faraday Transactions 2* **73**, 714 (1977).

[3] M. C. Marchetti, J. F. Joanny, S. Ramaswamy, T. B. Liverpool, J. Prost, M. Rao, and R. A. Simha, Hydrodynamics of soft active matter, *Reviews of Modern Physics* **85**, 1143–1189 (2013).

[4] K. J. Bishop, S. L. Biswal, and B. Bharti, Active colloids as models, materials, and machines, *Annual Review of Chemical and Biomolecular Engineering* **14**, 1–30 (2023).

[5] A. Barona Balda, A. Argun, A. Callegari, and G. Volpe, Playing with active matter, *American Journal of Physics* **92**, 847–858 (2024).

[6] D. Needelman and Z. Dogic, Active matter at the interface between materials science and cell biology, *Nature Reviews Materials* **2**, 17048 (2017).

[7] P. Pietzonka, E. Fodor, C. Lohrmann, M. E. Cates, and U. Seifert, Autonomous engines driven by active matter: Energetics and design principles, *Physical Review X* **9**, 041032 (2019).

[8] L. Tonks, The complete equation of state of one, two and three-dimensional gases of hard elastic spheres, *Physical Review* **50**, 955–963 (1936).

[9] T. Arnoux de Pirey, G. Lozano, and F. van Wijland, Active hard spheres in infinitely many dimensions, *Physical Review Letters* **123**, 260602 (2019).

[10] C. P. Royall, P. Charbonneau, M. Dijkstra, J. Russo, F. Smallenburg, T. Speck, and C. Valeriani, Colloidal hard spheres: Triumphs, challenges, and mysteries, *Reviews of Modern Physics* **96**, 045003 (2024).

[11] M. E. Cates and J. Tailleur, Motility-induced phase separation, *Annual Review of Condensed Matter Physics* **6**, 219–244 (2015).

[12] E. Fodor, C. Nardini, M. E. Cates, J. Tailleur, P. Visco, and F. van Wijland, How far from equilibrium is active matter?, *Physical Review Letters* **117**, 038103 (2016).

[13] R. J. Speedy, Cavities and free volume in hard-disc and hard-sphere systems, *Journal of the Chemical Society, Faraday Transactions 2* **77**, 329 (1981).

[14] R. J. Speedy, Cavities in one-dimensional fluids, *Journal of the Chemical Society, Faraday Transactions 2* **78**, 1645 (1982).

[15] R. J. Speedy and H. Reiss, Cavities in the hard sphere fluid and crystal and the equation of state, *Molecular Physics* **72**, 999 (1991).

[16] R. J. Speedy and H. Reiss, A computer simulation study of cavities in the hard disc fluid and crystal, *Molecular Physics* **72**, 1015 (1991).

[17] S. Sastry, T. M. Truskett, P. G. Debenedetti, S. Torquato, and F. H. Stillinger, Free volume in the hard sphere liquid, *Molecular Physics* **95**, 289–297 (1998).

[18] P. G. Debenedetti and T. M. Truskett, The statistical geometry of voids in liquids, *Fluid Phase Equilibria* **158–160**, 549–556 (1999).

[19] R. K. Bowles and D. S. Corti, Statistical geometry of hard sphere systems: exact relations for first-order phase transitions in multicomponent systems, *Molecular Physics* **98**, 429–438 (2000).

[20] A. P. Solon, Y. Fily, A. Baskaran, M. E. Cates, Y. Kafri, M. Kardar, and J. Tailleur, Pressure is not a state function for generic active fluids, *Nature Physics* **11**, 673–678 (2015).

[21] F. Mori, P. Le Doussal, S. N. Majumdar, and G. Schehr, Universal properties of a run-and-tumble particle in arbitrary dimension, *Physical Review E* **102**, 042133 (2020).

[22] B. Derrida, Microscopic versus macroscopic approaches to non-equilibrium systems, *Journal of Statistical Mechanics: Theory and Experiment* **2011**, P01030 (2011).

[23] R. Dandekar, S. Chakraborti, and R. Rajesh, Hard core run and tumble particles on a one-dimensional lattice, *Physical Review E* **102**, 062111 (2020).

[24] A straightforward way of numerically implementing a two-dimensional repulsive RTP (lattice) model is the four-direction RTP model introduced in [40].

[25] S. Sastry, D. S. Corti, P. G. Debenedetti, and F. H. Stillinger, Statistical geometry of particle packings.i.algorithm for exact determination of connectivity, volume, and surface areas of void space in monodisperse and polydisperse sphere packings, *Physical Review E* **56**, 5524–5532 (1997).

[26] E. Specht, A precise algorithm to detect voids in polydisperse circle packings, *Proceedings of the Royal Society A: Mathematical, Physical and Engineering Sciences* **471**, 20150421 (2015).

[27] R. Dwyer, The expected number of k-faces of a voronoi diagram, *Computers & Mathematics with Applications* **26**, 13–19 (1993).

[28] T. M. Truskett, S. Torquato, S. Sastry, P. G. Debenedetti, and F. H. Stillinger, Structural precursor to freezing in the hard-disk and hard-sphere systems, *Physical Review E* **58**, 3083–3088 (1998).

[29] P. Digregorio, D. Levis, A. Suma, L. F. Cugliandolo, G. Gonnella, and I. Pagonabarraga, 2d melting and motility induced phase separation in active brownian hard disks and dumbbells, *Journal of Physics: Conference Series* **1163**, 012073 (2019).

[30] B. J. Alder, W. G. Hoover, and T. E. Wainwright, Cooperative motion of hard disks leading to melting, *Physical Review Letters* **11**, 241–243 (1963).

[31] X. Xu and S. A. Rice, Maximally random jamming of one-component and binary hard-disk fluids in two dimensions, *Physical Review E* **83**, 021120 (2011).

[32] S. C. Takatori and J. F. Brady, Towards a thermodynamics of active matter, *Physical Review E* **91**, 032117 (2015).

[33] P. Gaspard and R. Kapral, Active matter, microreversibility, and thermodynamics, *Research* **2020**, 9739231 (2020).

[34] S. Cameron, M. Mosayebi, R. Bennett, and T. B. Liverpool, Equation of state for active matter, *Physical Review E* **108**, 014608 (2023).

[35] E. Schiltz-Rouse, H. Row, and S. A. Mallory, Kinetic temperature and pressure of an active tonks gas, *Physical Review E* **108**, 064601 (2023).

[36] J. O’Byrne, Y. Kafri, J. Tailleur, and F. van Wijland, Time irreversibility in active matter, from micro to macro, *Nature Reviews Physics* **4**, 167–183 (2022).

[37] J. U. Klamser, S. C. Kapfer, and W. Krauth, Thermodynamic phases in two-dimensional active matter, *Nature Communications* **9**, 5045 (2018).

[38] S. H. L. Klapp, Non-reciprocal interaction for living matter, *Nature Nanotechnology* **18**, 8–9 (2022).

[39] L. K. Davis, K. Proesmans, and E. Fodor, Active matter under control: Insights from response theory, *Physical Review X* **14**, 011012 (2024).

[40] T. Pietrangelo, C. Ybert, C. Cottin-Bizonne, and F. Detcheverry, Optimal run-and-tumble in slit-like confinement, *Physical Review Research* **6**, 023028 (2024).

[41] L. K. Davis (unpublished).

### Appendix A: Expressions for $p_{\rightarrow,\leftarrow}$ , $p_{\rightarrow,\rightarrow}$ and $p_{\leftarrow,\rightarrow}$ for $K \lesssim 1$ .

The expressions for  $p_{\rightarrow,\leftarrow}$ ,  $p_{\rightarrow,\rightarrow}$  and  $p_{\leftarrow,\rightarrow}$ , in the mean-field approximation, are determined through [23]

$$\begin{aligned} p_{\rightarrow,\leftarrow} &= \frac{2p_{\rightarrow,\rightarrow}\sqrt{K^2p_{\rightarrow,\rightarrow} + 2K + 1} - Kp_{\rightarrow,\rightarrow}^2}{Kp_{\rightarrow,\rightarrow} + 2}, \\ \frac{1}{\eta} &= \frac{(p_{\rightarrow,\leftarrow} + p_{\rightarrow,\rightarrow})(3Kp_{\rightarrow,\leftarrow} + Kp_{\rightarrow,\rightarrow} + 16) + 8K(2 - 2p_{\rightarrow,\leftarrow} - p_{\rightarrow,\rightarrow})}{8(p_{\rightarrow,\leftarrow} + p_{\rightarrow,\rightarrow})}, \\ p_{\leftarrow,\rightarrow} &= \frac{2p_{\rightarrow,\rightarrow}}{2 + 2K - p_{\rightarrow,\leftarrow} - p_{\rightarrow,\rightarrow}}, \end{aligned} \quad (\text{A1})$$

where  $K$  is the run length and  $\eta$  is the packing fraction. Expanding for small  $K \ll 1$  (up to  $\mathcal{O}(K^3)$ ) results in the directional probabilities in the weak-activity regime:

$$\begin{aligned} p_{\rightarrow,\leftarrow} &= \eta + \frac{\eta((3 - 4\eta + \eta^2)K}{2} \\ &\quad + \frac{\eta^2(4\eta^3 - 23\eta^2 + 41\eta - 22)K^2}{8}, \\ p_{\rightarrow,\rightarrow} &= \eta + \frac{\eta(1 - \eta)^2K}{2} + \frac{\eta^2(4\eta^3 - 15\eta^2 + 17\eta - 6)K^2}{8}, \\ p_{\leftarrow,\rightarrow} &= \eta + \frac{\eta(\eta^2 - 1)K}{2} + \frac{\eta(4 - 2\eta + \eta^2 - 7\eta^3 + 4\eta^4)K^2}{8} \end{aligned} \quad (\text{A2})$$

### Appendix B: Off-lattice exponential-tumble rate model of run-and-tumble particles (RTPs) in $d$ dimensions

We build a continuous, in space and time, run-and-tumble particle model. In the exponential running time model  $k_i$  is sampled from an exponential distribution. During the run phase a particle's orientation is fixed, whereas during a tumble event, occurring after  $k_i$  time since the last tumble, the orientation is randomly chosen on the sphere ( $\mathbb{S}^d$ ). The dynamics of the model is:

$$\begin{aligned} \dot{\mathbf{r}}_i(t) &= -\mu \nabla_i \phi(\{\mathbf{r}\}) + v_0(\delta(\tau_i(t) \bmod k_i) \hat{\mathbf{u}}_i(t) \\ &\quad + (1 - \delta(\tau_i(t) \bmod k_i)) \hat{\mathbf{u}}_i(s_i)), \\ \dot{\tau}_i &= 1, \quad \tau_i(t=0) \sim U(0, k_i), \\ \hat{\mathbf{u}}_i &\sim U(\mathbb{S}^d), \end{aligned} \quad (\text{B1})$$

where  $\tau_i$  is an internal clock variable which is initially a uniformly distributed variable,  $\phi(\{\mathbf{r}\})$  is the total potential energy imposing the repulsion between particles and

is defined as:

$$\phi = \frac{1}{2} \sum_{i,j}^N U(r_{ij}), \quad (\text{B2})$$

where  $r_{ij} \equiv |\mathbf{r}_i - \mathbf{r}_j|$  and  $U$  is the interaction pair potential given in WCA form:

$$U(r) = \left[ 4\varepsilon \left( \left( \frac{\sigma}{r} \right)^{12} - \left( \frac{\sigma}{r} \right)^6 \right) + \varepsilon \right] \Theta(2^{1/6}\sigma - r), \quad (\text{B3})$$

where  $\varepsilon$  is the repulsion strength,  $\sigma$  is the interaction range. The quantity  $\hat{\mathbf{u}}_i(t)$  in the dynamics is a vector uniformly distributed on the  $d$ -dimensional sphere at time  $t$ ,  $s_i$  is the last time particle  $i$  tumbled. The last two terms of the dynamics (B1) impose the running, when  $\tau_i$  is not a whole multiple of the  $k_i$ , and tumbling, otherwise. The passive (Markovian) limit is reached when  $K \rightarrow 0$ , ensuring uniformly distributed tumbles at every time increment.

### Appendix C: Off-lattice model of repulsive active Ornstein-Uhlenbeck particles (AOUPs) in $d$ dimensions

We obtain configurations of our system through the numerical solution of the dynamics of particle  $i$  reading as:

$$\begin{aligned} \dot{\mathbf{r}}_i &= -\mu \nabla_i \phi(\{\mathbf{r}\}) + \mathbf{v}_i, \quad \tau \dot{\mathbf{v}}_i = -\mathbf{v}_i + \sqrt{2D'} \mathbf{W}_i, \\ \langle \mathbf{W} \rangle &= 0, \quad \langle W_\alpha(t) W_\beta(s) \rangle = \delta_{\alpha,\beta}(t-s) \end{aligned} \quad (\text{C1})$$

where  $\dot{\mathbf{r}}_i$  is the instantaneous velocity of particle  $i$ ,  $\mu$  is the mobility,  $\mathbf{v}_i$  is the self propulsion governed by an Ornstein-Uhlenbeck process,  $\tau$  is the persistence time,

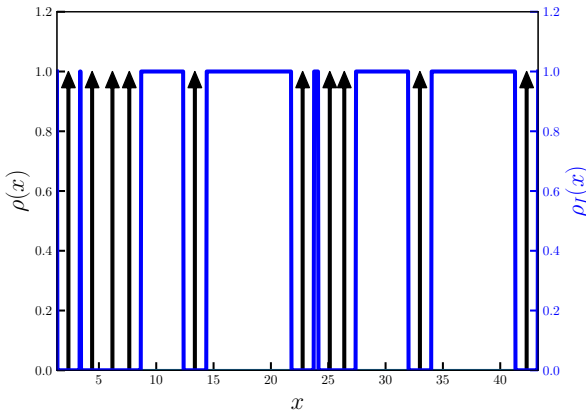


FIG. D.1. Plot showing the one-dimensional insertion profile  $\rho_I(x)$  (12) alongside the microscopic particle density  $\rho(x) = \sum_{i=1}^N \delta(x - x_i)$ .

$D'$  is the amplitude of the active noise, and  $\mathbf{W}_i$  is an independent gaussian white noise process.

#### Appendix D: Numerical simulations for the off-lattice models

In the numerical simulations of the off-lattice models, the dynamics (B1) and (C1) are numerically solved using the Euler-Maruyama method with timestep  $\delta t = 0.002$ . Initially the particles are distributed uniformly in a volume larger than the chosen  $V$  ( $V' > V(\eta)$ ) and then a pre-simulation is performed to drag the particles towards the origin until each particle is within  $V(\eta)$  and they are then made to relax according to equilibrium dynamics. For all simulations we impose periodic boundary conditions. Production runs begin, at the chosen activity parameter, once the distribution of particles is sufficiently uniform. We gather IS statistics every 1000 timesteps and our minimum threshold sample size is  $N_s = 5000$  at each  $K$ , or  $\tau$ , and  $\eta$ .

#### Appendix E: $\langle N_\Delta \Delta \rangle = \langle N_\Delta \rangle \langle \Delta \rangle$ ?

In general, beyond equilibrium, we show that one cannot write the averaged total insertion space as the product of the averaged number of insertion cavities and the averaged cavity size *if* the cavity size is first averaged per configuration  $\omega$  and only then averaged over all configurations  $\Omega$ . To show this we consider two notions of an average: a per-configuration-averaged mean ( $\omega$ -mean) and a total cavity-ensemble mean  $c$ -mean which are, re-

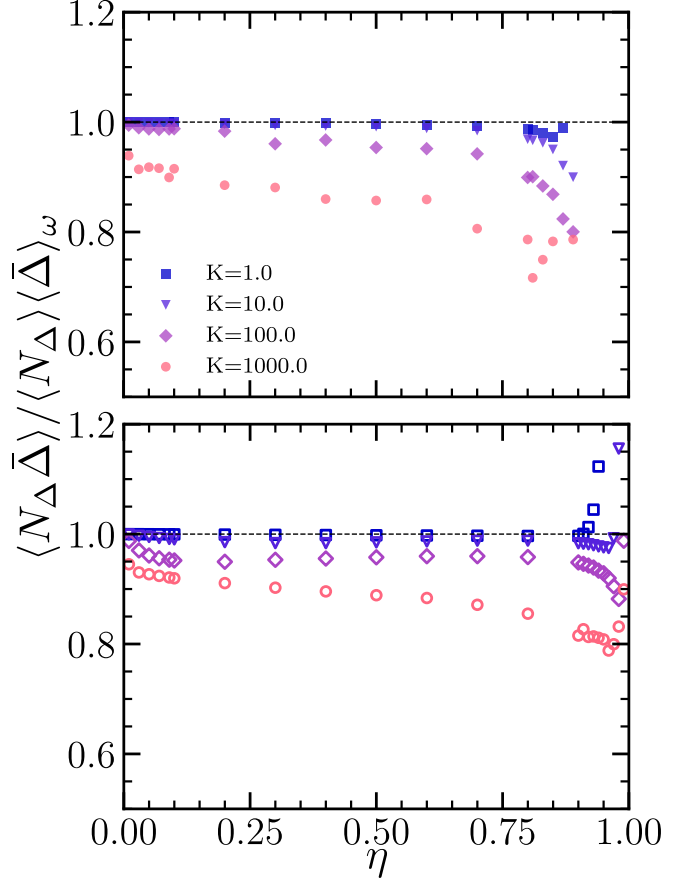


FIG. E.1. Plot showing the growing statistical dependence of  $N_\Delta$  and  $\bar{\Delta}$  for increased activity (higher  $K$ ) for off-lattice (top) and on-lattice (bottom) simulations of RTPs in  $d = 1$ . Close to equilibrium  $K = 1$  statistical independence is a valid assumption (besides very high packing fraction in the lattice data).

spectively, given as:

$$\langle \bar{\Delta} \rangle_\omega := \sum_{\omega}^{\Omega} p(\omega) \bar{\Delta}(\omega), \quad \bar{\Delta}(\omega) := \frac{\sum_{k=1}^{N_\Delta(\omega)} \Delta_k(\omega)}{N_\Delta(\omega)}, \quad (E1)$$

and

$$\langle \Delta \rangle := \frac{\sum_{\omega}^{\Omega} p(\omega) \sum_{k=1}^{N_\Delta(\omega)} \Delta_k(\omega)}{\sum_{\omega}^{\Omega} p(\omega) N_\Delta(\omega)} \equiv \frac{\langle V_I \rangle}{\langle N_\Delta \rangle}, \quad (E2)$$

where  $p(\omega)$  is the probability of the configuration  $\omega$ . Relation (E2) is exact and does not rely on statistical independence. However, if one computes  $\langle V_I \rangle$  from  $\langle \bar{\Delta} \rangle_\omega$  one requires the following:

$$\langle V_I \rangle = \langle N_\Delta \bar{\Delta} \rangle = \langle N_\Delta \rangle \langle \bar{\Delta} \rangle_\omega + \langle \langle N_\Delta \times \bar{\Delta} \rangle \rangle, \quad (E3)$$

where  $\langle \langle N_\Delta \times \bar{\Delta} \rangle \rangle := \langle N_\Delta \bar{\Delta} \rangle - \langle N_\Delta \rangle \langle \bar{\Delta} \rangle_\omega$  is the two-point connected correlation function. In equilibrium one can get away with  $\langle N_\Delta \bar{\Delta} \rangle = \langle N_\Delta \rangle \langle \bar{\Delta} \rangle_\omega$  due to the statistical independence of the number of cavities and the averaged (per configuration) cavity size (see Fig. E.1).

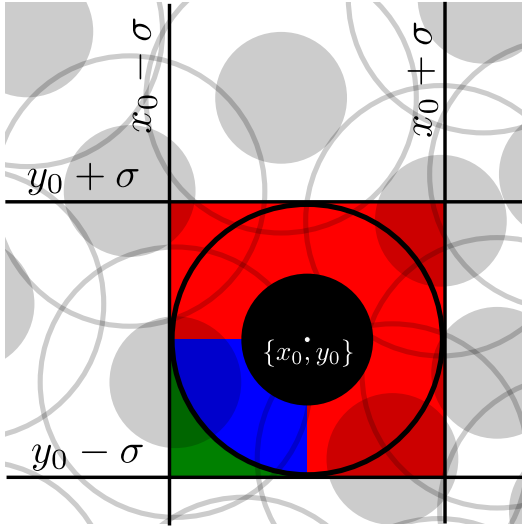


FIG. F.1. Schematic of how voxels are chosen to be removed due to the presence of one particle. The red box are voxels within the smallest square ( $d = 2$ ) encompassing the exclusion zone. Due to the symmetry of the circle and square only one (out of the four) quadrant requires attention, with the locations of the other excluded voxels obtained through trivial reflection and rotation (around  $\{x_0, y_0\}$ ) operations. Only those voxels within the exclusion zone need to be removed (blue voxels) leaving the rest (green voxels) remaining. After all particles have been checked, the union of the remaining green voxels is the insertion space up to the resolution  $l$ .

#### Appendix F: Method to determine the IS in $d = 2$

For a given configuration of discs  $\omega(t) := \{\mathbf{r}(t)\}$  the plane is discretized into voxels of side length  $l$  such that  $V^{1/2}/l \in \mathbb{Z}^+$ . Voxels are removed according to the following algorithm:

1. Input: particle coordinates  $\{(x_i, y_i)\}_{i=1}^N$ , voxel size  $l$ , box side lengths  $L_x, L_y$ .
2. Compute grid dimensions  $N_x = \lfloor L_x/l \rfloor$ ,  $N_y = \lfloor L_y/l \rfloor$ .
3. Initialize an empty set of voxel indices that should be removed:  $\mathcal{R} = \emptyset$ .
4. For each particle  $i$ :
  - (a) Form the particle-centered bounding interval in cell units: compute integer bounds  $n_{x-\sigma}, n_{x+\sigma}, n_{y-\sigma}, n_{y+\sigma}$  (see Fig. F.1). An example of an integer bounds can be computed as  $n_{x-\sigma} = \lceil ((x_0 - \sigma) - (-L_x/2))/l \rceil$ .
  - (b) Restrict loop over voxel indices to one quadrant of that bounding box, *e.g.*, from minima

$(x_0 - \sigma, y_0 - \sigma)$  up to the midpoint  $(x_0, y_0)$ , exploiting mirror symmetry.

- (c) For each candidate voxel  $(i_c, j_c)$  in that quadrant compute the squared distance  $(dr)^2 = (x(i_c) - x_0)^2 + (y(j_c) - y_0)^2$ , accounting for periodic images.
- (d) If  $(dr)^2 \leq (\frac{l}{2} + \sigma)^2$ , add the four symmetric cell indices (wrapped coordinates) to  $\mathcal{R}$ .
5. After all particles have been checked, compute the unique list  $\mathcal{R}^* = \{c_k | c_k \in \mathcal{R}\}$ .
6. Output:  $\mathcal{R}^*$ .

Then the insertion volume is determined as  $V_I = V - \sum_{k \in \mathcal{R}^*} l^2$ . To compute the individual insertion cavity sizes,  $\Delta$ 's, and numbers of insertion cavities,  $N_\Delta$ 's, we perform standard hierarchical clustering of the remaining voxels  $\notin \mathcal{R}^*$ . The criterion for voxel clustering is determined through nearest neighbor adjacency. Finally, the total insertion boundary  $S_I$  is computed based on the sum of the free edges of the insertion voxels forming the boundaries of the cavities. The cube shape of the voxels tends to result in higher  $S_I$ , to improve this in a deterministic way we “pythagorize” concave (inward facing) and convex (outward facing) corners of the cavity boundary. This involves replacing the two perpendicular lines that form the corner of two voxels with their hypotenuse. This technique is guaranteed to reproduce the exact  $S_I$  for  $l \rightarrow 0$  [41].

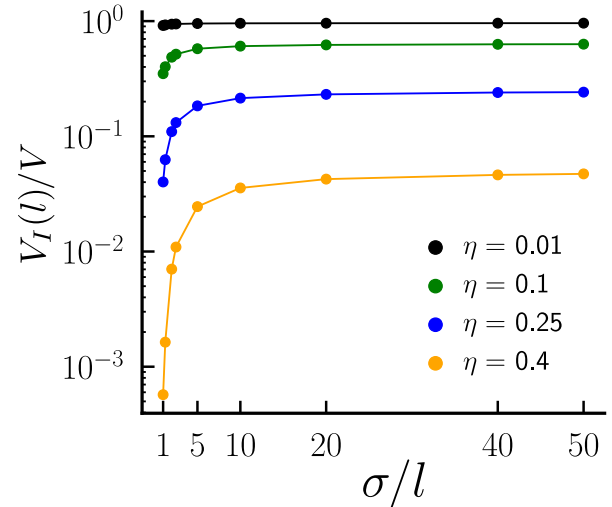


FIG. F.2. Convergence of the computed total insertion space as a function of  $\sigma/l$  for a configuration of hard discs at selected packing fractions.